Atmos. Chem. Phys. Discuss., 8, 15855–15899, 2008
www.atmos-chem-phys-discuss.net/8/15855/2008/


Atmospheric Chemistry and Physics Discussions

This discussion paper is/has been under review for the journal *Atmospheric Chemistry and Physics (ACP)*. Please refer to the corresponding final paper in *ACP* if available.

# Effects of sea surface winds on marine aerosols characteristics and impacts on longwave radiative forcing over the Arabian Sea

**Vijayakumar S. Nair**[1], **S. Suresh Babu**[1], **S. K. Satheesh**[2], **and K. Krishna Moorthy**[1]

[1]Space Physics Laboratory, Vikram Sarabhai Space Centre, Trivandrum, 695 022, India
[2]Centre for Atmospheric and Oceanic Science, Indian Institute of Sciences, Bangalore, India

Received: 3 June 2008 – Accepted: 22 July 2008 – Published: 20 August 2008

Correspondence to: S. Suresh Babu (s_sureshbabu@vssc.gov.in)

Published by Copernicus Publications on behalf of the European Geosciences Union.





## Abstract

Collocated measurements of spectral aerosol optical depths (AODs), total and BC mass concentrations, and number size distributions of near surface aerosols, along with sea surface winds, made onboard a scientific cruise over southeastern Arabian Sea, are used to delineate the effects of changes in the wind speed on aerosol properties and its implication on the shortwave and longwave radiative forcing. The results indicated that an increase in the sea-surface wind speed from calm to moderate (<1 to 8 m $s^{-1}$) values results in a selective increase of the particle concentrations in the size range 0.5 to 5 $\mu$m, leading to significant changes in the size distribution, increase in the mass concentration, decrease in the BC mass fraction, a remarkable increase in AODs in the near infrared and a flattening of the AOD spectrum. The consequent increase in the longwave direct radiative forcing almost entirely offsets the corresponding increase in the short wave direct radiative forcing (or even overcompensates) at the top of the atmosphere; while the surface forcing is offset by about 50%.

## 1 Introduction

Marine aerosols (both primary and secondary) play significant role in altering the radiation balance of the earth-atmosphere system at regional and global scales through the interaction with solar and terrestrial radiations, as well as in modifying the cloud microphysics. Sea salt aerosols formed by the action of winds on ocean surface, contribute nearly 19% to the global mean aerosol optical depth (AOD; Chin et al., 2002). It has been suggested that the increased sea salt generation due to the increase in wind speed resulting from the global warming would offset further warming (Latham and Smith, 1990). Effect of wind speed on the properties such as number concentration, mass concentration, scattering and extinction coefficients, and spectral optical depths of marine aerosols have been investigated in the past (e.g. Exton et al., 1985; Moorthy et al., 1997; Smirnov et al., 2003). A comprehensive summary of such attempts



ACPD

8, 15855–15899, 2008



and the reported results are available in an excellent review by Smirnov et al. (2002). However, size resolved measurements of wind-generated particles and the impacts on spectrally resolved AOD over marine environments are quite limited (Smirnov et al., 2002).

Marine aerosol system has mainly two components; produced in-situ and advected from the continents. Advection of continental aerosols (both anthropogenic as well as mineral dust) over to the oceanic environments have been extensively investigated earlier (e.g. Johansen and Hoffmann, 2003; Bates et al., 2004; Moorthy et al., 2005a; Zhu et al., 2007), and their role in causing spatial and temporal heterogeneity even over small oceanic regions have been highlighted with consequence on shortwave direct radiative forcing (Bates et al., 2006). These studies have shown that, in general, such advections lead to an increase in the atmospheric forcing efficiency of marine aerosols (Moorthy et al., 2005a). On the other hand wind borne sea salt aerosols are capable of offsetting these effects at least partially (Satheesh and Lubin, 2003).

The Arabian Sea, (oceanic region bound between 50° E to 77° E and 5° N to 22° N) plays a significant role in the weather and climate system of Asia and Africa through seasonally changing wind fields, which result in contrasting precipitation. The mean winds, that are weak easterlies or north-easterlies during winter and pre monsoon season (December to April) change to stronger south westerlies during the summer monsoon season (mid-May to September). During the former period, a weak anti-cyclone, located at ~15° N, favors an airmass that would bring-in continental aerosols from the mainlands of Asia (south and west) and north-eastern Africa over to the ocean and its confinement over the ocean, while during the latter period, the strong, moist marine airmass inducts coarse marine aerosols over to the adjoining continents thereby changing the aerosol properties over the mainland. This contrasting airmass types and associated changes in the aerosol environments cause heterogeneity (both spatial and temporal) in the aerosol characteristics and their radiative impacts (Moorthy et al., 2005a; Corrigan et al., 2006; Babu et al., 2007).

In this paper we present the details and results of an investigation on the effect of

changes in wind speed over the ocean on aerosols characteristics using collocated measurements of aerosol number size distribution, mass concentration, and spectral aerosol optical depth (AOD) onboard a research vessel over southeastern Arabian Sea. The results are used to identify the particle size regime, the concentrations at which are most affected and the wavelengths, the AODs at which are most influenced by the change in the average wind speed from calm to moderate conditions (<1 to 8 m $s^{-1}$). The measured aerosol properties are used to estimate the change in the longwave (IR, 8 to 12 $\mu$m) and shortwave (0.25 to 4 $\mu$m) direct radiative forcing, and examine the effect of increased winds on these.

## 2 Measurements, data, and analysis

Measurements of aerosol properties were made onboard Oceanographic Research Vessel Sagar Kanya (SK) during its cruise SK219, over the southeastern Arabian Sea centered around a small oceanic region (at 72°39′ E; 8°17′ N) from 18 April to 7 May, 2005. The ship sailed off from the port of Kochi (Fig. 1) on 18 April and reached the study region on 19 April. This small region, identified by a point in a rectangle in Fig. 1, is bound between 72°30′ E and 72°48′ E in longitude and 8°10′ N and 8°24′ N in latitude. Over this region the ship made several zigzag tracks as shown in the blowup. After measurements, the ship reached Kochi on 7 May. Because of its very small spatial extent, the observations made over the study region can be considered as a time series observation. Same time, the measurements from 18 to 19 April (ship moving off Kochi to the study region) and from 6 to 7 May (returning to Kochi) provide information on the spatial variation. Collocated measurements of aerosol parameters, made onboard the ORV, comprised of columnar spectral aerosol optical depth (AOD), columnar water vapor ($W$), mass concentrations ($M_T$) of composite (total) and ($M_B$) of black carbon aerosols, and number concentration ($N(r)$) of the composite aerosols in the size (diameter) range 0.3 to 20 $\mu$m in 15 size bins.

Spectral AODs, columnar ozone and water vapor ($W$) were measured using a Micro-




tops sunphotometer and ozone monitor (Solar Light Co, USA). While the sunphotometer yielded AODs at five wavelengths (340, 380, 500, 675, and 870 nm), the ozone monitor provided column-integrated ozone, W and AOD at 1020 nm. The details of Microtops, principle of AOD estimation, precautions while using onboard ship and error budget are given in detail in several papers (e.g. Porter et al., 2001; Moorthy et al., 2005a) and hence are not repeated. Latitude, longitude and time information are fed to the Microtops using GPS receivers attached to each instrument. During each measurement, a set of three observations was made in quick succession and the least among these AODs is taken as the representative value. Measurements were done when the solar disc and its neighborhood was free from visible clouds. The instrument was calibrated at the factory in the beginning of 2005, prior to the campaign.

An aethalometer (AE-21 Magee Scientific, USA) was used to measure the black carbon mass concentration ($M_B$) continuously and at near-real-time using optical attenuation technique at 880 nm. The change in optical attenuation due to the aerosol loading on its quartz filter tape is calibrated in terms of $M_B$ using an effective specific mass absorption cross section of 16.6 $m^2\,g^{-1}$, which incorporates a factor of 1.9 for the amplification due to multiple scattering in the filter tape (C factor, e.g. Weingartner et al., 2003). Intrinsic problems associated with aethalometer measurements are shadowing effect, multiple scattering in the filter tape, and uncertainties in the specific absorption cross section (Weingartner et al., 2003; Arnott et al., 2005; Corrigan et al., 2006), which lead to an uncertainty of ~20%. Nevertheless, it is a rugged instrument, extremely convenient for field measurements. Inter-comparison of $M_B$ measured using the aethalometer with several other techniques have shown reasonably good agreement with the average values agreeing within the experimental errors (e.g. Hitzenberger et al., 2006). In the present setup the instrument was operated continuously, round the clock, at a flow rate of 3 l per minute (LPM), and timebase of 5 min. The ambient air was drawn from a height ~3 m above the top deck of the ship.

Mass concentration ($M_T$) of total suspended particulates was measured using a High Volume Sampler (Handi vol, USA). Desiccated, pre-weighed, quartz fiber filter was



ACPD
8, 15855–15899, 2008



exposed to an ambient airflow (567 LPM) for three to four hours. The substrate was then removed, kept in a marked, self-locking cover and desiccated. Aerosol mass concentration ($M_T$) was calculated from the difference ($\Delta m$) between the masses of the tare and loaded filter determined using a microbalance.

$$M_T = \frac{\Delta m}{V \Delta t} \quad (1)$$

where $V$ is the flow rate and $\Delta t$ is the duration of sampling. The flow rate was calibrated prior to the cruise and its consistency was ensured after the cruise.

Number size distribution of total aerosols was measured using the Optical Particle Counter (OPC Model 1.108 Grimm, Germany). The instrument (http://www.grimm-aerosol.com) provides size resolved number concentration of particles in the size range 0.3 to 20 $\mu$m diameter in 15 size channels, based on light scattering principle. The instrument was operated in its outdoor weather proof housing, which controlled the relative humidity (RH) of the sampling air to 60%. Ambient temperature and RH were measured using sensors attached to the instrument housing.

## 3 Meteorological parameters during the cruise

Supplementary meteorological data provides important information on prevailing synoptic and local conditions. While the NCEP (National Centers for Environmental Prediction) reanalysis data were used for the synoptic winds, the local meteorological parameters were monitored using shipboard sensors.

### 3.1 Synoptic winds

Synoptic winds, at 850 hPa over the study region, are shown in Fig. 2 based on the NCEP reanalysis data. The region of measurements is shown as a rectangle in the figure. The low level anti-cyclonic circulation is located at ~15° N, 62° E in the central Arabian Sea, with the study area towards its rim to the southeast. The resulting flow



ACPD
8, 15855–15899, 2008



pattern yields weak, northerly/northwesterly winds around the region, and northeasterly winds further to its west; while to the north of ~17° N the flow is generally stronger and westerly over the ocean, changing to northwesterly at the coast. Consequently the low level winds reaching the ship have quite long history over the ocean.

### 3.2 Local meteorology

The temporal variations of air temperature, relative humidity, wind speed, and direction, from the onboard measurements, are shown in Fig. 3 (panels respectively from the top to bottom). These data, obtained as 20 min averages, are smoothed using a 6-h running mean to suppress the short-term variations. From the figure it can be seen that the low-level winds (middle panel) were weak (<3 m s$^{-1}$) until 25 April. Thereafter, the speed increased gradually, reaching up to ~6.5 m s$^{-1}$ (the 20 min averages going as high as 8.2 m s$^{-1}$) by 30 April and decreased after 2 May. Wind direction was generally varying and was from north/northwest from 24 April onwards. The RH was ~73% during the initial part of the cruise until 29 April and decreased thereafter to lower values (68 to 70%). Air temperature remained between 28 and 30°C.

## 4 Results

### 4.1 Aerosol optical depth and Angstrom parameters

Temporal variations of the daily mean AODs, at the 6 wavelengths (340, 380, 500, 675, 870 and 1020 nm), during the campaign period are shown in Fig. 4. The horizontal arrow in the figure shows the period when the ship was at the study region, where the measurements could be approximated to a time series (and beyond this the spatial variation too could be important). High AODs (~0.42 at 500 nm) are observed at the port of Kochi. As the ship moved off, the AOD (at 500 nm) increased initially to ~0.55 and then decreased sharply to reach the lowest value of ~0.22 (at 500 nm) by 21 April.



ACPD
8, 15855–15899, 2008



Subsequently the AODs increased steadily to reach a peak value (0.4 at 500 nm) by 30 April to 2 May period and then dropped off. The rapid decrease off Kochi is mainly due to the decreasing source impact. Kochi is one of the busiest ports on the west coast (after Mumbai) and is also a rapidly growing urban centre. The city also has several small and medium scale industries, beside a large oil refinery and a fertilizer factory. Thus, there is significant amount of anthropogenic activity. The vast inland water bodies (lakes) and ocean to the west keep the environment highly humid and warm. All these could be contributing to the high AODs near to the coast and rapid fall as we move off. The average AODs (at 500 nm) were 0.48±0.04 near to the coast. Compared to this the AOD was lower in the time series region, with a mean value of 0.29±0.01 for the period 21 April–6 May.

Spectral dependence of AOD could be related to the columnar particle size distribution through the Angstrom equation

$$\tau_P(\lambda)=\beta\lambda^{-\alpha} \quad (2)$$

where $\alpha$ is a measure of the ratio of abundance of accumulation mode (sub micron) to the coarse mode (super micron) particles and $\beta$ is the turbidity coefficient indicative of the total loading. Both, $\alpha$ and $\beta$ are estimated for each AOD spectrum from the regression slope and intercept of the graph connecting $\tau_P(\lambda)$ (AOD) and $\lambda$ in log-log scale. The temporal variations (daily mean) of $\alpha$ and $\beta$ are shown in Fig. 5. At the port and close to it, $\alpha$ remained high (1.2 to 1.5) primarily due to the fine (accumulation mode) particle dominance. As the ship reached the study region, $\alpha$ increases sharply to reach the highest value of ~1.7 by 24 April and then dropped off gradually to reach ~0.5 by 1 May, before increasing later. This change is more temporal than spatial. The final increase on 6 May occurred as the ship started approaching Kochi. During the same period, $\beta$ decreased continuously as we moved away from the port, and then remained around the low value of ~0.1 until 28 April. Subsequently, it increased sharply to reach the highest value of ~ 0.3 by 2 May. During this period $\alpha$ became the lowest (unlike close to the port) implying a drastic change in the aerosol size spectrum and abundance. These changes are episodic, as the ship was confined only to the study



ACPD
8, 15855–15899, 2008



region and it is interesting to note that the extreme values of $\alpha$ and $\beta$ were observed far from the main land.

### 4.2 Number concentration

With a view to examining any signature of the changes in the columnar AODs and $\alpha$ on the ambient (near surface) aerosol concentration and size distribution, we analyzed the OPC data. In Fig. 6, the temporal variations of the daily mean aerosol number concentration are shown for 3 different size ranges. These are obtained by averaging the size resolved number density measurements, made using the OPC, in daily ensembles. The ordinate scale on the left represents the number concentration of all the stages; i.e., particles with size >0.3 $\mu$m ($N_{0.3}$), while the right hand side ordinate represents those for particles larger than 0.65 $\mu$m ($N_{0.65}$) and 0.8 $\mu$m ($N_{0.8}$). The rationale behind this was to examine the behavior of the coarser mode particles vis-à-vis with the changes of $\alpha$ and $\beta$ in Fig. 5.

In-line with the earlier observations, number densities in all sizes decreased rapidly as the ship moved off Kochi and tend to recover after 5 May, when the ship started approaching the mainland. In the oceanic region, represented by the graph for the period 21 April to 5 May, the total number density ($N_{0.3}$) does not show any perceptible change. However, the $N_{0.65}$ and $N_{0.8}$ reached a minimum by 24 April and increased steadily to reach a peak around 30 April to 1 May (similar to the AODs) and then gradually fell off. The higher channels of the OPC representing still coarser particles also showed similar behavior. At the peak, the concentrations are ~3 to 4 times higher than the values seen on 24 April or 4 May. The variations of the coarse mode concentrations are very much similar in nature, but differing in phase, to those seen in $\alpha$ and $\beta$. When $\alpha$ reached the peak (1.7) and $\beta$ the trough (0.07) on 24 April, $N_{0.65}$ and $N_{0.8}$ also were at their lowest values. Thereafter $N_{0.65}$ and $N_{0.8}$ increased steadily, so too $\beta$; but $\alpha$ decreased. The minimum in $\alpha$ (0.5) and peak in $\beta$ (0.33) occur on 1 May, while $N_{0.65}$ and $N_{0.8}$ peaked during 30 April–1 May. Thereafter the number density of the coarse mode particles decreased, so too $\beta$. This clearly shows that the changes in



ACPD
8, 15855–15899, 2008



the spectral characteristics of the columnar AODs over the oceanic area were well associated with those occurring in the number size distribution of aerosols in the marine atmospheric boundary layer (MABL).

### 4.3 Mass concentrations of BC and total aerosols

Temporal variations of the mass concentrations ($M_T$) of total suspended particle, estimated using the high volume sampler and shown in Fig. 7, revealed very high values (~40 $\mu g\,m^{-3}$) at the mainland (Kochi), and decreasing rapidly towards open ocean. BC also behaved almost similarly, with a high value (>2 $\mu g\,m^{-3}$) at the coast and decreasing steeply to far oceanic region. In order to focus only on the variations over the far ocean, we have restricted the figure only to the period when the ship was at the time series location. From the high values at the coast, $M_T$ and $M_B$ decrease steeply to reach their lowest values during the cruise (~12 $\mu g\,m^{-3}$ and ~0.3 $\mu g\,m^{-3}$, respectively) by 22/23 April. Subsequently there is a weak increase in $M_B$, which reaches ~0.6 $\mu g\,m^{-3}$ (which is still less than the coastal values by a factor of >3) and fluctuated around that value during 26 April to 6 May. On the other hand, $M_T$ increased, initially gradually by a factor of 2, and then steeply to reach the peak value of ~40 $\mu g\,m^{-3}$(which is comparable to that measured at and near the coast) on 1 May, before dropping off to very low values subsequently. This sharp peak from 26 April to 1 May is similar to the behavior of $\beta$ in Fig. 5 and that of $N_{0.65}$ and $N_{0.8}$ in Fig. 6.

This indicates that whatever has caused the increase in $M_T$ and $N_C$ during 24 April to 1 May and resulted in a corresponding increase in AOD and $\beta$ and decrease in $\alpha$, did not contribute significantly to BC and the fine mode concentration. As a result the percentage of share ($F_{BC}$) of BC to total aerosol mass showed the lowest value (~1.5%) during this period. It is also important to note that $F_{BC}$ was quite high (4.5%) on 24 April when AOD, $\beta$ and $M_T$ were the lowest and $\alpha$ the highest. This large variation (by a factor of ~3) of $F_{BC}$ over the small study area with in the short period implies significant changes in the aerosol properties and thus forcing efficiencies (e.g. Babu et al., 2004).



ACPD
8, 15855–15899, 2008



## 5 Discussion

Aerosols over the Arabian Sea, like over any oceanic region impacted by adjoining continents, would mainly consist of

i) sea salt aerosols (in coarse and accumulation regimes) produced in situ by the sea surface winds (e.g. Gong, 2003),

ii) continental aerosols (mainly in accumulation mode regime) advected from the (Indian) sub continent by favorable winds (e.g. Ramanathan et al., 2001), and

iii) transported mineral dust from the adjoining arid regions of West Asia (e.g. Johansen and Hoffmann, 2003; Moorthy et al., 2005a).

In addition there will be certain contribution due to non-sea-salt sulphate aerosols in the fine particle regime associated with DMS emissions (Shenoy et al., 2002). The relative abundance of each of these species at a given time will strongly depend on the regional meteorological conditions; mainly the prevailing wind fields (Moorthy et al., 1997). Examining our results (Figs. 3 to 7), change in the winds appears to be the potential candidate leading to the temporal changes in aerosol properties over the study regions. This could be due to the in situ production of sea-salt or advection of mineral dust or both.

### 5.1 Advection pathways

Airmass back trajectory analyses show potential pathways for aerosol transport and are widely used to qualitatively assess the change in aerosol properties associated with different airmasses coming from distinct source regions (Bates et al., 2004). HYbrid Single Particle Legrangian Integrated Trajectory (HYSPLIT) model (Draxler and Rolph, 2003) of NOAA is used to estimate the five-day back trajectories reaching the observation site at two different altitudes representative of regions within the MABL (500 m); and free troposphere (3600 m), following Moorthy et al. (2005a). The mass



ACPD
8, 15855–15899, 2008



plots of these trajectories are shown in Fig. 8 for the entire campaign period. At 500 m level, the trajectories arrived mainly along the west coast of peninsular India except on 21 to 24 April. Free tropospheric trajectories showed the influence of Indian peninsula and Bay of Bengal during the first few days (17 April to 20 April), then shifted towards the East (21 April to 29 April) and finally to the west (30 April to 06 May). Interestingly, airmass back trajectories during 21 to 25 April at both the levels showed advection from the east/northeast (south BoB/Northern Indian Ocean). These are shown by the dotted lines in Fig. 8. During these days, the trajectories go well back (~100° E) over the BoB at higher levels. There after the trajectories shifted to the western Arabian Sea and remained confined to the oceanic regions, thereby indicating that advection of mineral aerosols was rather insignificant during this period when the aerosol parameters showed a consistent increase. This leaves the in situ production of sea salt aerosols by the strong winds as the potential candidate for the observed changes.

### 5.2 Wind speed dependence

In the light of the above, we examined the measured aerosol properties vis-à-vis with the average wind speeds measured onboard the ORV.

#### 5.2.1 Aerosol optical depth

A scatter plot of the daily average wind speed and daily mean AOD at the two extreme wavelengths, 340 nm and 1020 nm, used in the measurements is shown in Fig. 9. In both the cases a general increase in AOD is observed with increase in the wind speed, the association appears to be stronger at 1020 nm. To quantify this, we parameterized the wind speed dependence of AOD, following Moorthy et al. (1997) using the analytical equation of the form

$$\tau_\lambda(U)=\tau_{0\lambda}e^{b_\tau(\lambda)U} \quad (3)$$

where $\tau_\lambda(U)$ the daily mean AOD at the wavelength $\lambda$ for the mean wind speed $U$, $\tau_{0\lambda}$ the AOD for zero wind speed (or wind speed independent AOD) at the same wave-



ACPD
8, 15855–15899, 2008



length and $b_\tau(\lambda)$ is the index of wind speed dependence or simply the wind index and is considered to be wavelength dependent (Moorthy et al., 1997; Satheesh, 2002). Equation (1) suggests a linear increase in $\ln \tau$ with $U$ and the regression line drawn through the points are also shown in Fig. 9, which shows a higher slope ($b_\tau$) and better correlation at 1020 nm. The results of similar parameterization, performed for all the wavelengths, are given in Table 1, which shows a consistent increase in $b_\tau$ with $\lambda$. The wind index $b_\tau$and the correlation coefficient $R_\lambda$ are significantly higher at the longest wavelength 1020 nm, compared to 340 nm, where as $\tau_{0\lambda}$ is lower. The scatter (deviation from the regression line) also decreases towards longer wavelengths (as evidenced by $R$) implying that the effect of increase in wind speed on AOD is spectrally selective with the near IR wavelengths being more sensitive. This suggests a change in the shape of the AOD spectrum with wind speed; the spectra tending to be flatter at higher wind speeds, leading to lower values of $\alpha$. The values of $\alpha$ and $\beta$, estimated from the daily mean AODs and using Eq. (2), were grouped into ensembles of mean wind in an ascending order. The variations of the ensemble averaged $\alpha$ and $\beta$ with ensemble mean wind speed are shown in Fig. 10. While $\alpha$ decreases with increase in $U$ indicating the flattening of the AOD spectrum (due to the selective enhancement of coarse mode particles), $\beta$ increases suggesting increase in columnar abundance of aerosols.

#### 5.2.2 Number concentration and size distribution

The size resolved number concentrations measured by the OPC facilitated closer examination of the wind speed effect on aerosols and to delineate the size ranges that are most sensitive to wind speed changes. During the cruise, the (OPC measured) number size distributions were available at 5 min intervals and these showed significant day-to-day variations, sometimes even within a day also. As such, we considered the 6 h average of number concentrations and wind speed. In Fig. 11, we show the scatter plot for 3 cases, each one progressively focusing to coarser size regime as we move through the panels from the top to bottom. The top most panel examines the to-



ACPD
8, 15855–15899, 2008



tal concentrations (of all particles with sizes >0.3 $\mu$m, $N_{0.3}$), the middle one considers only particles with diameter >0.65 $\mu$m ($N_{0.65}$) and the bottom one for concentration of particles with diameter >2.0 $\mu$m. In all the panels ordinate is the number concentration in log scale and the abscissa is the wind speed (both averaged for 6 h). In each panel, the solid line is the regression fit to the Eq. (4).

$$N_r(U) = N_{r0} e^{b_N(r)U} \quad (4)$$

Due to the size selective nature of sea-spray production (Gong, 2003), the increase in wind speed results in the change in the size distribution of aerosols, as particles in certain size spectrum are produced in larger abundance. This is incorporated in Eq. (4) by treating $b_N$ as a function of $r$. It is seen from Fig. 11 that the slope of the regression line and correlation coefficient increases with increase in particle size. Performing the regression analysis (as discussed earlier) for each of the 15 size channels of the OPC, we estimated wind index ($b_N$) and correlation coefficient ($R$) for different size ranges covered by the OPC and its variation with particle diameter is examined in Fig. 12. The corresponding regression coefficients are also plotted in the same figure, which very clearly demonstrates size dependence of wind index $b_N$. Both $b_N(r)$ and $R$ are very low for particle diameter less than 0.5 $\mu$m and greater than 5 $\mu$m. Particle concentration in the size range (diameter) 0.7 to 3 $\mu$m are most susceptible to the wind speed changes. Decrease in both $R$ and $b$ below 0.5 $\mu$m is due to the decrease in the production rate and also due to the presence of non sea salt particles, while at larger sizes the residence time becomes very important.

Investigations (in the past) on the response of aerosol concentration in the MABL to wind speed over the oceans have shown that increased sea-spray production contributes to particle concentration at radii $r$>0.2 $\mu$m (Gras and Ayers, 1983) and maximum contribution occurs at $r$~1 to 2 $\mu$m (Fitzgerald, 1991). Even though the efficiency of sea-spray production reduces largely in the sub micron regime compared to non sea salt sources (Gong, 2003), O'Dowd et al. (1997) have reported sea-spray contribution to fine particle regime with a broad mode at ~0.2 $\mu$m having a $\sigma$ of 2. Due to the higher residence time, these fine particles continue to contribute longer even after the high



ACPD
8, 15855–15899, 2008



winds have subsidized. The dependence of $b_N$ on particle size has been discussed earlier by Smith et al. (1989), O'Dowd and Smith (1993) and Nilsson et al. (2001), but most of them were limited to the coarse mode regime.

The selective enhancement in the production of sea salt aerosols by winds would influence the surface and volume size distributions as well. This is examined by estimating the effective radius, defined as the ratio of the third moment over the second moment of the size distribution

$$R_{\text{eff}} = \frac{\int r^3 n(r) dr}{\int r^2 n(r) dr} \tag{5}$$

An examination of $R_{\text{eff}}$ versus wind speed, revealed a linear increase in $R_{\text{eff}}$ with $U$ with a regression slope of 0.07 at a correlation coefficient of 0.58 (Fig. 13).

### 5.2.3 Total mass concentration

A scatter plot of the total mass concentration ($M_T$) from the HVS measurements against the daily mean wind speed $U$ shown in Fig. 14, also reveals an exponential increase in $M_T$ with $U$ conforming to the relation,

$$M_T(U) = M_{T_o} e^{b_M U} \tag{6}$$

where $M_{T0}$ is the wind speed independent component and $b_M$ is the index of wind speed dependence. Despite that $M_T$ measurements were limited to 3 to 4 h a day, it followed Eq. (6) with a correlation coefficient of 0.73, while the regression coefficients yielded $M_{T0}=11.2\pm1\,\mu g\,m^{-3}$ and $b_M=0.24\pm0.06\,s\,m^{-1}$. The increase in aerosol mass concentration associated with increase in wind speed over ocean has been extensively investigated in the past (e.g. Lovett, 1978; Exton, 1985; Moorthy et al., 2005b; Ganguly et al., 2005). A compilation of the values of $b_M$ observed in the earlier investigations is given in Table 2, along with the current estimates. From the table it is clear that the wind index vary significantly over the oceanic regions depending on the ocean-atmosphere condition and advection of aerosols (dust as well as anthropogenic). The very low



ACPD
8, 15855–15899, 2008



value (0.05) reported by Satheesh et al. (1999) is mainly attributed to the advection of anthropogenic aerosols to the Indian Ocean, while the high b values were associated with the dust transport.

### 5.3 Vertical homogeneity

The properties of ambient aerosols are always amenable to perturbations caused by the dynamics of the MABL; though it would be weaker over the ocean compared to the landmass. However, when the perturbations are strong and of greater spatial extent associated with regional scale weather, it is possible that the changes occur over most of the vertical column, so that both the column and MABL behave similarly and there exists a vertical homogeneity. To examine this, we have plotted in Fig. 15, the temporal variations of the coarse mode AOD ($\tau_{coarse}$) and the fine mode fraction (FMF) derived from the Moderate Resolution Imaging Spectroradiometer (MODIS) data (as the mean of Aqua and Terra) along with the number concentration $N_{0.65}$ deduced from the OPC measurements. A three-fold increase in coarse mode AOD is observed during the transition from the fine dominated period (calm wind conditions) to coarse mode dominated period (moderate wind conditions), with a simultaneous decrease in the FMF from 0.85 to 0.6. Thus the increase in wind speed has resulted in not only the increase in particle abundance, but also change in size distribution leading larger increase in the AOD at near infra red and a decrease in the Angstrom exponent. In the following we estimate the implications of these on aerosol direct radiative forcing in the short wave and long wave regime.

### 5.4 Implications to direct radiative forcing

Aerosol direct radiative forcing (DRF) is the first order estimation of the climate impact due to the atmospheric aerosols. It represents the change ($\Delta F$) in the solar radiative flux either at the top of the atmosphere (TOA), the surface, or within the atmosphere



ACPD
8, 15855–15899, 2008



due to the interaction with aerosols. So that

$$(\Delta F)_{\mathrm{TOA},S}=(F_{NA})_{\mathrm{TOA},S}-(F_A)_{\mathrm{TOA},S} \quad (7)$$

where $F_A$ and $F_{NA}$ are the net fluxes with and without aerosols. Difference between the TOA and surface forcing yields the atmospheric forcing. DRF is strongly dependent on the aerosol spectral AOD ($\tau_\lambda$), spectral single scattering albedo ($\omega_\lambda$), and the scattering phase function ($P(\theta)$), as well as on the surface albedo and meteorological conditions.

For the estimation of both shortwave (SW, 0.25 to 4.0 $\mu$m) and longwave (LW, 4.0 to 50.0 $\mu$m) DRF, we followed the widely used empirical cum modeling approach (e.g. Satheesh and Srinivasan, 2002; Satheesh and Lubin, 2003; Markowicz et al., 2003; Babu et al., 2004; Moorthy et al., 2005a). This essentially consists of adopting a zero-order aerosol model from Hess et al. (1998) and varying the relative abundance of its constituents, keeping the observational data as the constraints, such that the modified model reproduces the measured AOD spectrally, within measurement errors. The resulting model, though cannot be considered unique, gives an equivalent aerosol model reproducing the observed columnar optical properties. Based on the AOD and $F_{\mathrm{BC}}$, we selected the "marine polluted" model; the constituents of which are water soluble, soot, sea salt (accumulation and coarse modes), and transported mineral dust. Keeping $F_{\mathrm{BC}}$, $M_T$, and $\alpha$ as constraints, the concentrations of the species were adjusted to reproduce the spectral AODs within the measurement errors. The modeled values of $\omega_\lambda$ and $P(\theta)$ along with the measured $\tau(\lambda)$ and $\alpha$ were used as inputs to the radiative transfer model SBDART (Santa Barbara DISORT Atmospheric Radiative Transfer model; Ricchiazzi et al., 1998) and the diurnally averaged, clear sky, radiative fluxes at the TOA and surface were estimated. Similarly fluxes reaching the TOA and surface for aerosol free conditions were also simulated and using the Eq. (7) both shortwave radiative forcing (SWRF) and longwave radiative forcing (LWRF) were estimated.

Unlike SWRF, LWRF strongly depends on the vertical profiles of temperature and relative humidity (Lubin et al., 2002; Huang et al., 2007), columnar water vapor and ozone content (Hollweg et al., 2006) and surface temperature. Realistic vertical profiles



ACPD
8, 15855–15899, 2008



of temperature and water vapor were taken from the radiosonde observations from the island Minicoy (8.3° N, 73.04° E) (location shown in Fig. 1) close to the study area. During the cruise, standard tropical atmospheric profiles used in the SBDART showed an excellent agreement with measured profiles within the measurement uncertainties. As such, we used the measured profiles upto 30 km (the maximum altitude of the sondes) and above that standard tropical profiles from SBDART were used. Column integrated water vapor and ozone content, measured onboard using the Microtops and hourly measured sea surface temperature (SST) were also fed to the model for the more realistic LW flux estimations. We estimated the AOD at 10 $\mu$m using the aerosol model described above and it was found to be ~20% of the AOD measured at 500 nm, which is consistent with the observations of Markowicz et al. (2003). Extensive sensitivity analyses have shown that nearly 87% of the LWRF is in the middle infrared atmospheric window region (8–12 $\mu$m) (Vogelmann et al., 2003; Hollweg et al., 2006) and as such, we focused only on this region.

In view of distinct aerosol properties observed during this campaign, we considered 2 extreme cases, Case 1 (21 April to 29 April) corresponding to high $\alpha$ and low aerosol concentrations and Case 2 (30 April to 05 May) characterized by low values of $\alpha$ and high aerosol loading. Corresponding aerosol properties measured/retrieved and modeled are given in Table 3. From the discussions forgone, it is clear that Case 1 corresponds to calm wind condition and Case 2 represents moderate wind condition. The SWRF estimated for these two cases are shown in the top panel of Fig. 16. Transition from Case 1 to Case 2 resulted in an increase in the absolute magnitude of the TOA forcing by ~1 W m$^{-2}$ and surface forcing by 7.8 W m$^{-2}$ in the SW regime. During Case 2 period of moderate winds, we have observed large increase in the concentration of coarse mode aerosols at the surface as well as in column. Comparison of LWRF estimated for this period and fine mode aerosols dominated calm period (Case 1) is shown in the bottom panel of Fig. 16. Change from the calm to moderate wind condition increases the LWRF from +0.23 to +1.9 at TOA while at the surface the forcing increased from +0.35 to +3.5 W m$^{-2}$. The significance of this observation is



ACPD
8, 15855–15899, 2008



not a mere 8 to 10 fold increase in the LWRF, but more importantly the increase in LWRF is more than the corresponding increase in the magnitude of SWRF. SWRF and LWRF have contrasting impacts on the radiation balance; generally the former cools the surface and warms the atmosphere while latter warms the surface and cools the atmosphere. Under normal conditions, the magnitude of the LWRF is far less in comparison to the SWRF and is even negligible over the fine mode aerosols dominated regions. However, when the dominance of coarse mode aerosols becomes significant, such as over oceans or deserts, LWRF can significantly offset the SWRF (Ackerman and Chung, 1992). During Case 2 of our study, LWRF offsets ~23% of the SWRF at the TOA and ~15% at the surface. Compilations of LWRF and SWRF over oceanic regions are given in Table 4, in which the offsetting effect of LWRF on SWRF is also given in percentage. Almost all studies suggest nearly 10 to 25% offsetting of SWRF at the surface and TOA. During ACE Asia, LWRF of 1 to 10 $W\,m^{-2}$ was observed at the surface (Vogelmann et al., 2003) and it is comparable to the values reported from the Indian Ocean during INDOEX (Lubin et al., 2002). Uncertainties do exist due to the lack of information on the microphysical properties of aerosols in the IR region. Nevertheless, the large balancing of the SWRF by LWRF (which is primarily due to natural aerosols) is very important in the radiative equilibrium of earth atmosphere system

Sensitivity analyses have shown that the accuracy of the estimated SWRF depends mainly on the accuracy of the measured aerosol properties and land surface reflectance (Podgorny et al., 2000). However such detailed examination of the sensitivity of LWRF to the aerosol properties as well as meteorological conditions are limited (Lubin et al., 2002, Marckowicz et al., 2003; Hollweg et al., 2006). LWRF (at TOA and surface) decreases with the increase in water vapor content and the rate of decrease is much higher for surface forcing. An increase from 1 to 3 $g\,cm^{-2}$ (in columnar water vapor content) will reduce the surface DRF from 11.5 to 6 $W\,m^{-2}$ and TOA DRF from 4.27 to 4.03 $W\,m^{-2}$ (Marckowicz et al., 2003). A change of ±10 K throughout the temperature profile leads to a change of 1.8 $W\,m^{-2}$ in the surface LWRF over an urban location over India (Panicker et al., 2008). However, change in vertical profiles of wa-



ACPD
8, 15855–15899, 2008



ter accounts nearly 25% variations in the effective longwave emissivity (Dupont et al., 2008).

## 6 Conclusions

Collocated measurements of several aerosol parameters were carried out onboard a research vessel in a small region of the southeastern Arabian Sea, off the west coast of India for about a month during the inter monsoon season of 2005. The data are used to examine the changes in aerosol properties associated with wind fields and the consequence on infrared radiative forcing vis-à-vis the shortwave forcing. Our investigation showed that

1. All the aerosol parameters, mass and number concentration in the marine atmospheric boundary layer (MABL) as well as columnar spectral AODs, increased exponentially with increase in the mean wind speed, though through different extents.

2. For increase in wind speed from calm ($< 1\,m\,s^{-1}$) to moderate ($\sim 8\,m\,s^{-1}$) conditions, number concentration of particles (in the MABL) in the size range 0.5 $\mu$m to 3 $\mu$m was found to be most influenced, while the increase in AODs was higher in the near infrared wavelengths.

3. This selective enhancement of the coarse mode particles due to sea salt led to an increase in the coarse mode AODs,flattening of the AOD spectrum and a decrease in the fine-mode fraction.

4. The consequent increase in the infrared (10 to 12 $\mu$m) direct radiative forcing was found to offset the corresponding increase in the short wave direct forcing by more than 100% at the top of the atmosphere and 50% at the surface.

*Acknowledgements.* The work was carried out under the Geosphere Biosphere Programme of the Indian Space Research Organization (ISRO-GBP). The authors thank the Indian Climate





Research Program for providing the opportunity for this experiment. We thank G. S. Bhat for providing the meteorological data relevant for this study. We gratefully acknowledge NOAA-CIRES Climate Diagnostics Center, Boulder, Colorado, for the NCEP-NCAR reanalysis data. We acknowledge NOAA Air Resources Laboratory for the provision of the HYSPLIT transport and dispersion model and READY website (http://www.arl.noaa.gov/ready.html) used in this publication.

## References

Arnott, W. P., Hamasha, K., Moosmuller, H., Sheridan, P. J., and Ohren, J. A.: Towards aerosol light-absorption measurements with a 7-wavelength aethalometer: evaluation with a photoacoustic instrument and 3-wavelength nephelometer, Aerosol Sci. Technol., 39(1), 17–29, 2005.

Babu, S. S., Moorthy, K. K., and Satheesh, S. K.: Aerosol black carbon over Arabian Sea during intermonsoon season and summer monsoon season, Geophys. Res. Lett., 31, L06104, doi:10.1029/2003GL018716, 2004.

Bates, T. S., Anderson, T. L., Baynard, T.,, et al.: Aerosol direct radiative effects over the northwest Atlantic, northwest Pacific, and North Indian Oceans: estimates based on in-situ chemical and optical measurements and chemical transport modeling, Atmos. Chem. Phys., 6, 1657–1732, 2006, http://www.atmos-chem-phys.net/6/1657/2006/.

Bates, T. S., Quinn, P. K., Coffman, D. J., Covert, D. S., Miller, T. L., Johnson, J. E., Carmichael, G. R., Guazzotti, S. A., Sodeman, D. A., Prather, K. A., Rivera, M., Russell, L. M., and Merrill, J. T.: Marine boundary layer dust and pollution transport associated with the passage of a frontal system over eastern Asia, J. Geophys. Res., 109, D19, doi:10.1029/2003JD004094, 2004.

Chin, M., Ginoux, P., Kinne, S., Holben, B. N., Duncan, B. N., Martin, R. V., Logan, J. A., Higurashi, A., and Nakajima, T.: Tropospheric aerosol optical thickness from the GOCART model and comparisons with satellite and sunphotometer measurements, J. Atmos. Sci. 59, 461–483, 2002.

Corrigan, C. E., Ramanathan, V., and Schauer, J. J.: Impact of monsoon transitions





on the physical and optical properties of aerosols, J. Geophys. Res., 111, D18208, doi:10.1029/2005JD006370, 2006.
Draxler, R. R. and Rolph, G. D.: HYSPLIT (Hybrid Single Particle Lagrangian Integrated Trajectory) model access, available at: http://www.arl.noaa.gov/ready/hysplit4.html, 2003.
Dupont, J.-C., Haeffelin, M., Drobinski, P., and Besnard, T.: Parametric model to estimate clear-sky longwave irradiance at the surface on the basis of vertical distribution of humidity and temperature, J. Geophys. Res., 113, D07203, doi:10.1029/2007JD009046, 2008.
Exton, H. J., Latham, J., Park, P. M., Perry, S. J., and Smith, M. H.: The production and dispersal of marine aerosol, Q. J. Roy. Meteorol. Soc., 111, 817–837, 1985.
Fitzgerald, J. W.: Marine Aerosols: a review, Atmos. Environ., 25A, 533–545, 1991.
Ganguly, D., Jayaraman, A., and Gadhavi, H.: In situ ship cruise measurements of mass concentration and size distribution of aerosols over Bay of Bengal and their radiative impacts, J. Geophys. Res., 110, D06205, doi:10.1029/2004JD005325, 2005.
Gong, S. L.: Parameterization of sea salt aerosol source function for sub and super micron particles, Global Biogeochem. Cy., 17, 4, 1097, doi:10.1029/2003GB002079, 2003.
Gras, J. L. and Ayers, G. P.: Marine aerosol at southern mid-latitudes, J. Geophys. Res., 88, 10 661–10 666, 1983.
Hess, M., Koepke, P., and Schult, I.: Optical properties of aerosols and clouds: The software package (OPAC), B. Am. Meteorol. Soc., 79, 831–844, 1998.
Hitzenberger, R., Petzold, A., Bauer, H., Ctyroky, P., Pouresmaeil, P., Laskus, L., and Puxbaum, H.: Intercomparison of thermal and optical measurement methods for elemental carbon and black carbon at an urban location, Environ. Sci. Technol., 15, 40(20), 6377–6383, 2006.
Hollweg, H.-D., Bakan, S., and Taylor, J. P.: Is the aerosol emission detectable in the thermal infrared?, J. Geophys. Res., 111, D15202, doi:10.1029/2005JD006432, 2006.
Huang, Y., Ramaswamy, V., and Soden, B.: An investigation of the sensitivity of the clear-sky outgoing longwave radiation to atmospheric temperature and water vapor, J. Geophys. Res., 112, D05104, doi:10.1029/2005JD006906, 2007.
Johansen, A. M. and Hoffmann, M. R.: Chemical characterization of ambient aerosol collected during the northeast monsoon season over the Arabian Sea: Labile-Fe(II) and other trace metals, J. Geophys. Res., 108(D14), 4408, doi:10.1029/2002JD003280, 2003.
Latham, J. and Smith, M. H.: Effect on global warming of wind-dependent aerosol generation at the ocean surface, Nature, 347, 372–373, 1990.
Lovett, R. F.: Quantitative measurement of airborne sea-salt in the Northern Atlantic, Tellus, 30,





358–364, 1978.
Lubin, D., Satheesh, S. K., McFarquar, G., and Heymsfield, A. J.: Longwave radiative forcing of Indian Ocean tropospheric aerosol, J. Geophys. Res., 107(D19), 8004, doi:10.1029/2001JD001183, 2002.
Markowicz, K. M., Flatau, P. J., Vogelmann, A. M., Quinn, P. K., and Welton, E. J.: Clear sky infrared aerosol radiative forcing at the surface and the top of the atmosphere, Q. J. Roy. Meteorol. Soc., 129, 2927–2947, 2003.
Moorthy, K. K., Satheesh, S. K., and Murthy, B. V. K.: Investigations of Marine Aerosols over the Tropical Indian Ocean, J. Geophys. Res., 102, 18 827–18 842, 1997.
Moorthy, K. K., Babu, S. S., and Satheesh, S. K.: Aerosol Characteristics and Radiative Impacts over the Arabian Sea during the Intermonsoon Season: Results from ARMEX Field Campaign, J. Atmos. Sci., 62(1), 192–206, 2005a.
Moorthy, K. K., Satheesh, S. K., Babu, S. S., and Saha, A.: Large latitudinal gradients and temporal heterogeneity in aerosol black carbon and its mass mixing ratio over southern and northern oceans during a trans-continental cruise experiment, Geophys. Res. Lett., 32, L14818, doi:10.1029/2005GL023267, 2005b.
Nilsson, E. D., Rannik, U., Swietlicki, E., Leek, C., Aalto, P. P., Zhou, J., and Norman, M.: Turbulent aerosol fluxes over the Arctic Ocean 2. Wind-driven sources from the sea, J. Geophys. Res., 106(D23), 32 139–32 154, 2001.
O'Dowd, C. D. and Smith, M. H.: Physicochemical properties of aerosols over the Northeast Atlantic: Evidence for wind-speed-related submicron sea-salt aerosol production, J. Geophys. Res., 98(D1), 1137–1149, 1993.
O'Dowd, C. D., Smith, M. H., Consterdine, I. E., and Lowe, J. A.: Marine aerosol, sea-salt and the marine sulphur cycle: a short review, Atmos. Environ., 31, 73–80, 1997.
Panicker, A. S., Pandithurai, G., Safai, P. D., and Kewat, S.: Observations of enhanced aerosol longwave radiative forcing over an urban environment, Geophys. Res. Lett., 35, L04817, doi:10.1029/2007GL032879, 2008.
Podgorny, I. A., Conant, W. C., Ramanathan, V., and Satheesh, S. K.: Aerosol modulation of atmospheric and surface solar heating rates over the tropical Indian Ocean, Tellus B, 53, 947–958, 2000.
Porter, J. N., Miller, M., Pietras, C., and Motell, C.: Ship based sun photometer measurements using Microtops sun photometer, J. Atmos. Oceanic Technol., 18, 765–744, 2001.
Ramachandran, S. and Jayaraman, A.: Premonsoon aerosol loading and size distribu-





tion over the Arabian Sea and the Tropical Indian Ocean, J. Geophys. Res., 107, 4738, doi:10.1029/2002JD002386, 2002.
Ramanathan, V., Crutzen, P. J., Lelieveld, J., Mitra, A. P., Althausen, D., et al.: Indian Ocean experiment: an integrated analysis of the climate forcing and effects of the great Indo-Asian haze, J. Geophys. Res., 106(D22), 28 371–28 398, doi:10.1029/2001JD900133, 2001.
Ricchiazzi, P., Yang, S., Gautier, C., and Sowle, D.: SBDART: a Research and Teaching Software Tool for Plane-Parallel Radiative Transfer in the Earth's Atmosphere, B. Am. Meteorol. Soc., 79, 2101–2114, 1998.
Satheesh, S. K. and Lubin, D.: Short wave versus long wave radiative forcing by Indian Ocean aerosols: role of sea-surface winds, Geophys. Res. Lett., 30, 13, doi:10.1029/2003GL017499, 2003.
Satheesh, S. K. and Srinivasan, J.: Enhanced aerosol loading over Arabian Sea during the pre-monsoon season: Natural or anthropogenic?, Geophys. Res. Lett., 29, 18, doi:10.1029/2002GL015687, 2002.
Satheesh, S. K., Moorthy, K. K., Kaufman, Y. J., and Takemura, T.: Aerosol optical depth, physical properties and radiative forcing over the Arabian Sea, Meteorol. Atmos. Phys., 91, 45–62, 2006.
Satheesh, S. K., Ramanathan, V., Jones, X. L., Lobert, J. M., Podgorny, I. A., Prospero, J. M., Holben, B. N., and Loeb, N. G.: A Model for Natural and Anthropogenic Aerosols over the Tropical Indian Ocean Derived from INDOEX data, J. Geophys. Res., 104(D22), 27 421–27 440, 1999.
Satheesh, S. K.: Aerosol radiative forcing over tropical Indian Ocean: Modulation by sea surface winds, Curr. Sci., 82, 310–316, 2002.
Shenoy, D. M., Joseph, S., Dileep Kumar, M., and George, M. D.: Control and inter-annual variability of dimethyl sulfide in the Indian Ocean, J. Geophys. Res., 107(D19), 8008, doi:10.1029/2001JD00371, 2002.
Smirnov, A., Holben, B. N., Eck, T. F., Dubovik, O., and Slusker, I.: Effect of wind speed on columnar aerosol optical properties at Midway Island, J. Geophys. Res., 108(D24), 4802, doi:10.1029/2003JD003879, 2003.
Smirnov, A., Holben, B. N., Kaufman, Y. J., Dubovik, O., Eck, T. F., Slutsker, I., Pietras, C., and Halthore, R. N.: Optical properties of atmospheric aerosol in maritime environments, J. Atmos. Sci., 59, 501–523, 2002.
Smith, M. H., Consterdine, I. E., and Park, P. M.: Atmospheric loadings of marine aerosol during





Hebridean cyclone, Q. J. Roy. Meteorol. Soc., 115, 383–395,1989.
Tsunogai, S., Saito, O., Yamada, K., and Nakaya, S.: Chemical composition of oceanic aerosol, J. Geophys. Res., 77, 5283–5291, 1972.
Vogelmann, A. M., Flatau, P. J., Szczodrak, M., Markowicz, K. M., and Minnett, P. J.: Observations of large aerosol infrared forcing at the surface, Geophys. Res. Lett., 30(12), 1655, doi:10.1029/2002GL016829, 2003.
Weingartner, E., Saathoff, H., Schnaiter, M., Streit, N., Bitnar, B., and Baltensperger, U.: Absorption of light by soot particles: determination of the absorption coefficient by means of aethalometers, J. Aerosol Sci., 34, 1445–1463, 2003.
Zhu, A., Ramanathan, V., Li, F., and Kim, D.: Dust plumes over the Pacific, Indian, and Atlantic oceans: Climatology and radiative impact, J. Geophys. Res., 112, D16208, doi:10.1029/2007JD008427, 2007.





**Table 1.** The wind index ($b_\tau$) estimated at different wavelengths. $R$ is the correlation coefficient and $\tau_0$ is the AOD for zero wind speed.

| $\lambda$ (nm) | $b_\tau$ (s m$^{-1}$) | $R$ | $\tau_0$ |
|---|---|---|---|
| 340 | 0.10±0.05 | 0.55±0.2 | 0.30 |
| 380 | 0.12±0.05 | 0.61±0.2 | 0.26 |
| 500 | 0.13±0.05 | 0.59±0.2 | 0.18 |
| 675 | 0.19±0.07 | 0.63±0.2 | 0.096 |
| 870 | 0.22±0.08 | 0.631±0.3 | 0.071 |
| 1020 | 0.23±0.07 | 0.73±0.2 | 0.047 |



ACPD
8, 15855–15899, 2008



**Table 2.** A compilation of the values of wind index ($b_M$) observed in the earlier investigations along with the current estimates.

| No | Region | $b_M$(s m$^{-1}$) | Reference |
|---|---|---|---|
| 1 | Atlantic Ocean | 0.16 | Lovett (1978) |
| 2 | Pacific Ocean | 0.62 | Tsunogai et al. (1972) |
| 3 | Atlantic Ocean | 0.17 | Exton et al. (1985) |
| 4 | Kaashidhoo Indian Ocean | 0.05 | Satheesh et al. (1999) |
| 5 | Southern Ocean | 0.18 | Moorthy et al. (2005b) |
| 6 | Bay of Bengal | 0.17 | Ganguly et al. (2005) |
| 7 | Arabian Sea and tropical Indian Ocean | 0.35 | Ramachandran and Jayaraman (2002) |
| 8 | Arabian Sea | 0.24 | Present study |



ACPD
8, 15855–15899, 2008



**Table 3.** Aerosol parameters measured or retrieved for two cases considered in the study.

| | $\tau_{500}$ | $\alpha$ | $SSA_{500}$ | $F_{BC}$ | SW DRF | | | LW DRF | | |
|---|---|---|---|---|---|---|---|---|---|---|
| | | | | | TOA | Surface | Atmos | TOA | Surface | Atmos |
| Case 1 | 0.24±0.05 | 1.38±0.3 | 0.918 | 3.03±0.9 | −6.9 | −15.6 | +8.7 | +0.23 | +0.35 | −0.12 |
| Case 2 | 0.32±0.06 | 0.86±0.2 | 0.889 | 2.07±0.4 | −8.1 | −23.4 | +15.3 | +1.9 | +3.5 | −1.6 |

**Table 4.** Compilation of short wave radiative forcing and long wave radiative forcing over oceanic regions.

| Region and period | SW TOA | SW SUR | LW TOA | LW SUR | TOA (%) | SUR (%) | Reference |
|---|---|---|---|---|---|---|---|
| Southern AS (SMS) | −9.1 | −13.1 | 1.3 | 5.2 | 14.28 | 39.69 | Satheesh et al. (2006) |
| Southern AS (WMS) | −6 | −12 | 0.8 | 4.2 | 13.33 | 35 | Satheesh et al. (2006) |
| Southern AS, April-May 2005 | −8.1 | −23.4 | 1.9 | 3.5 | 23.45 | 14.95 | Present study |
| Indian Ocean, March 2001 | −6.8 | −10.1 | 1.2 | 4.3 | 17.64 | 42.57 | Vinoj et al. (2004) |
| Arabian Sea, March 2001 | −5.9 | −18.9 | 1.7 | 6.4 | 28.81 | 33.86 | Vinoj et al. (2004) |
| BoB, February 2003 | −11.58 | −29.5 | 0.97 | 2.94 | 8.37 | 9.94 | Ganguly et al. (2005) |
| Indian Ocean, INDOEX | −10 | −30 | 1.3 | 7.7 | 13 | 25.66 | Lubin et al. (2002), Satheesh and Ramanathan (2000) |
| Sea of Japan, 2001 | −12.7 | −26.1 | 1.5 | 4.6 | 11.81 | 17.62 | Markowicz et al. (2003) |
| Indian Ocean | −12.5 | −35.6 | 2 | 10 | 16 | 28.08 | Satheesh and Lubin (2003) |





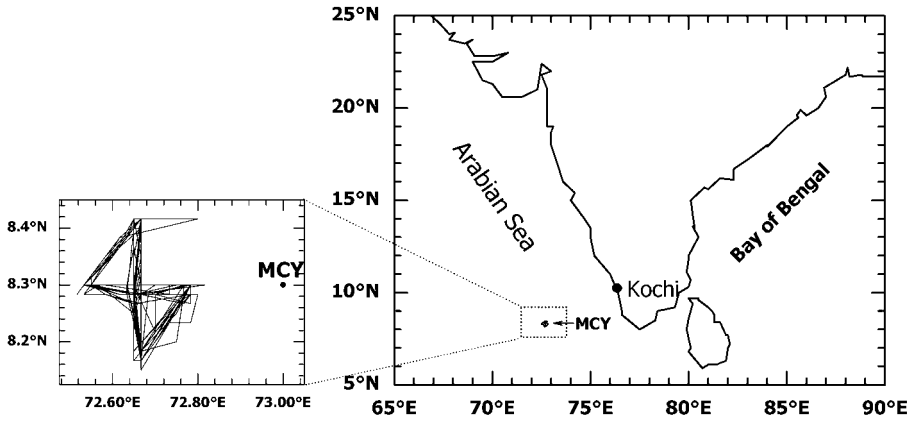


**Fig. 1.** ARMEX IIA measurement site is drawn in a rectangle on the right panel. The major port (Kochi) near to the site is also shown. Closer view of the ship transit made during the observation period is given in the left panel.



ACPD
8, 15855–15899, 2008



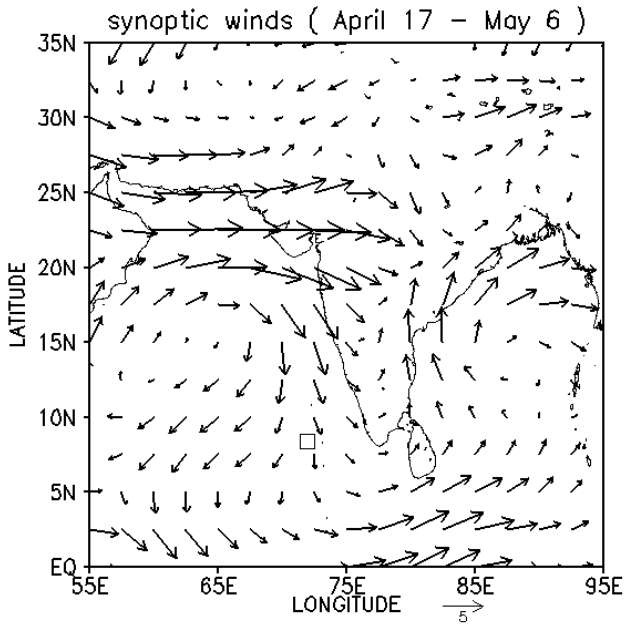


**Fig. 2.** Synoptic wind pattern over the measurement region during 17 April to 7 May and the measurement site is shown as rectangle.



ACPD

8, 15855–15899, 2008



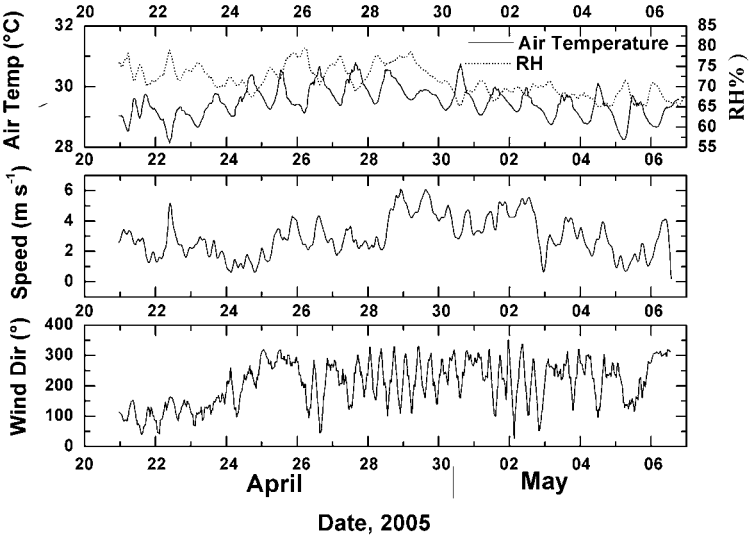


**Fig. 3.** Time series measurements of air temperature, humidity, wind speed and direction during 20 April to 6 May 2005.



ACPD
8, 15855–15899, 2008



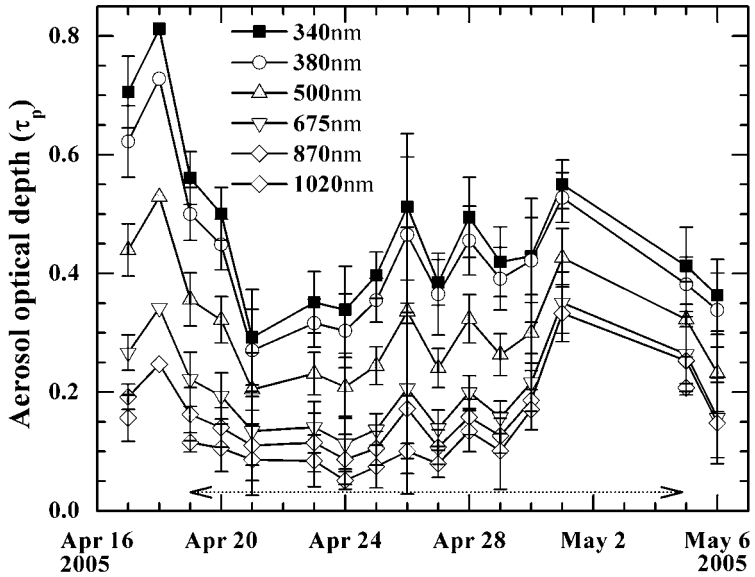


**Fig. 4.** Temporal variation of AOD at 6 wavelengths for the entire campaign period is shown and the measurements over the study area are marked by a horizontal line.



ACPD
8, 15855–15899, 2008



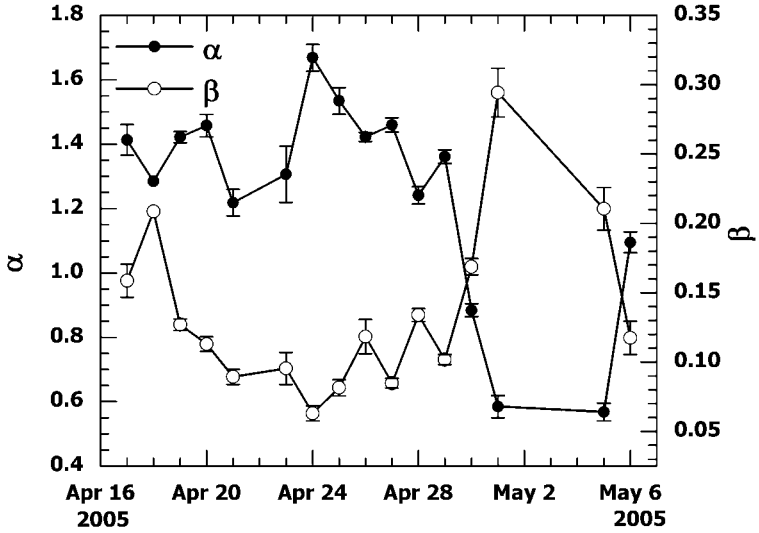


**Fig. 5.** Mean daily variation of angstrom exponent ($\alpha$) and turbidity coefficient ($\beta$) are shown along the left and right ordinate, respectively.



ACPD
8, 15855–15899, 2008



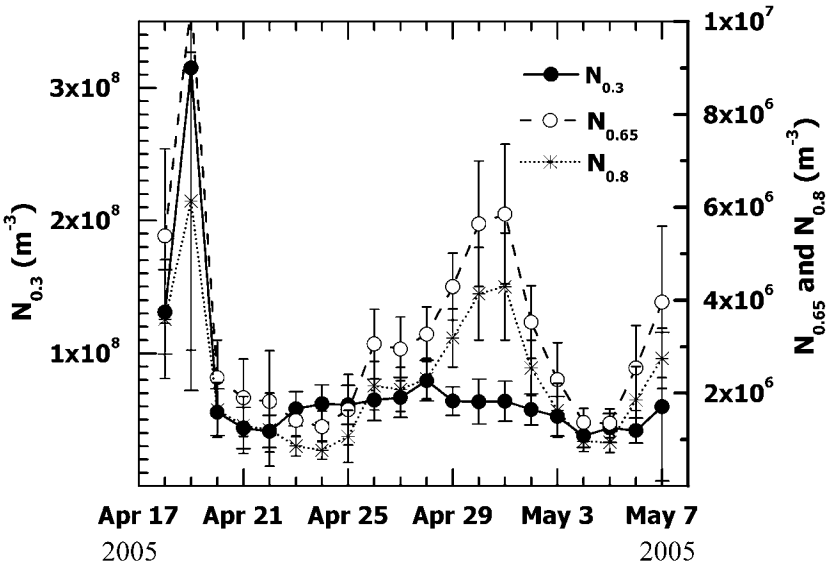


**Fig. 6.** Temporal variation of mean daily number concentration of particle diameter greater than 0.3 $\mu$m ($N_{0.3}$) on the left ordinate, number concentrations of particle diameter greater than 0.65 $\mu$m ($N_{0.65}$) and 0.8 $\mu$m ($N_{0.8}$) are shown in the right ordinate.



ACPD
8, 15855–15899, 2008



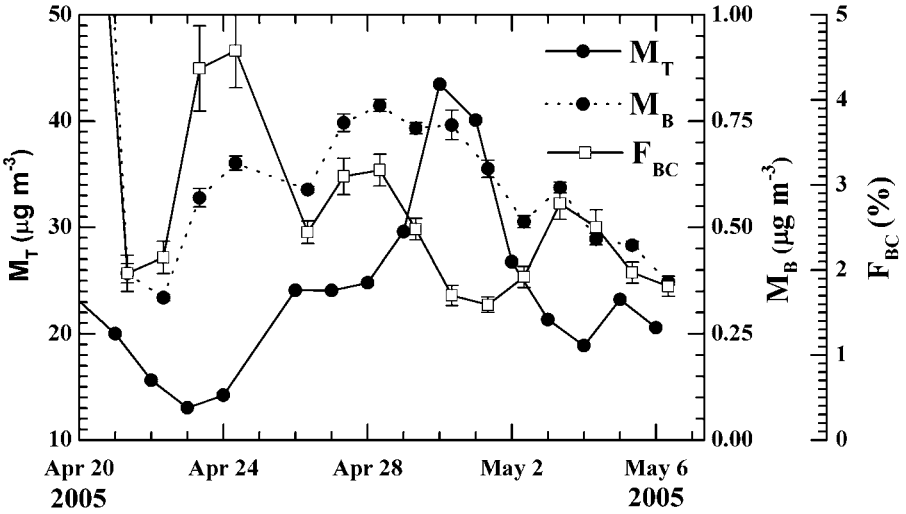


**Fig. 7.** Mean daily variation of total mass concentration ($M_T$) along the left ordinate, BC mass concentration ($M_{BC}$) and BC mass fraction ($F_{BC}$) are shown along the right ordinate.



ACPD
8, 15855–15899, 2008



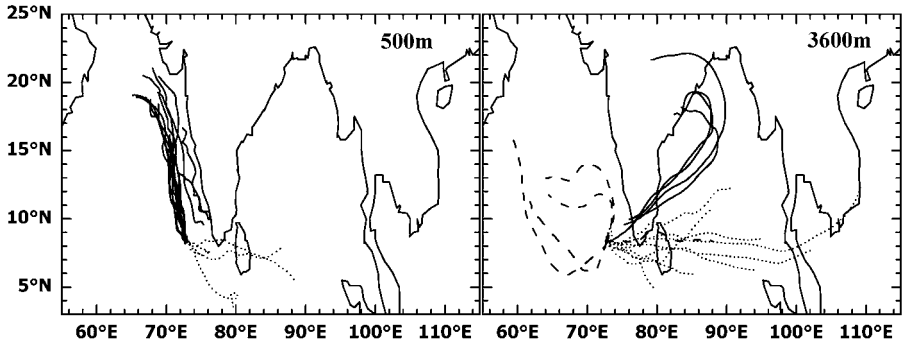


**Fig. 8.** HYSPLIT five day air mass back trajectories for the campaign period at 500 m, and 3600 m height are shown in three panels. Trajectories having East Asian (dotted lines) and Arabian Sea (dashed lines) influence are identified distinctly from others in the figure.



ACPD
8, 15855–15899, 2008



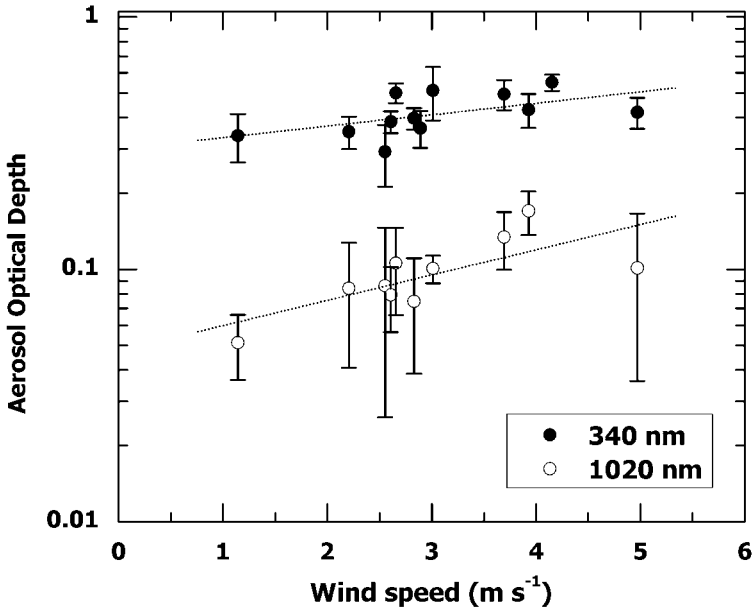


**Fig. 9.** Scatter diagram of aerosol optical depth at 500 nm ($\tau_{500}$) and 1020 nm ($\tau_{1020}$) versus wind speed in log-linear scale.



ACPD
8, 15855–15899, 2008



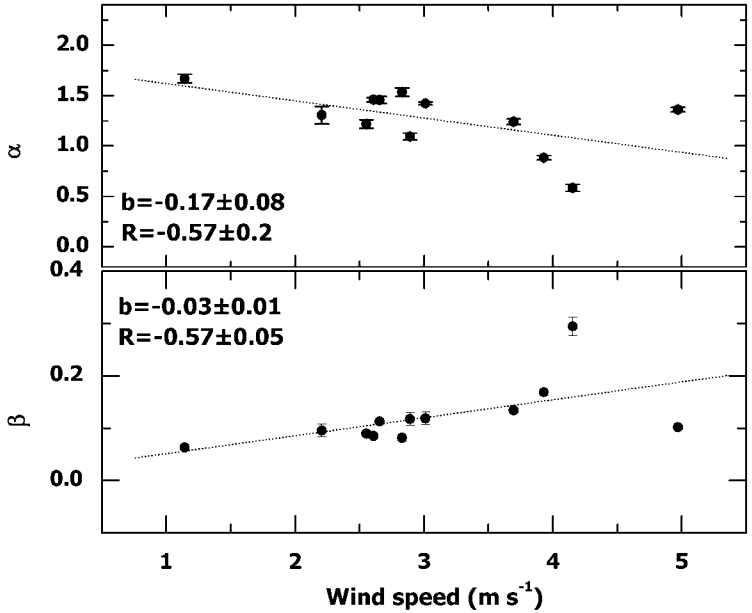


**Fig. 10.** Wind speed dependence of angstrom parameters $\alpha$ (top panel) and $\beta$ (bottom panel).



ACPD
8, 15855–15899, 2008



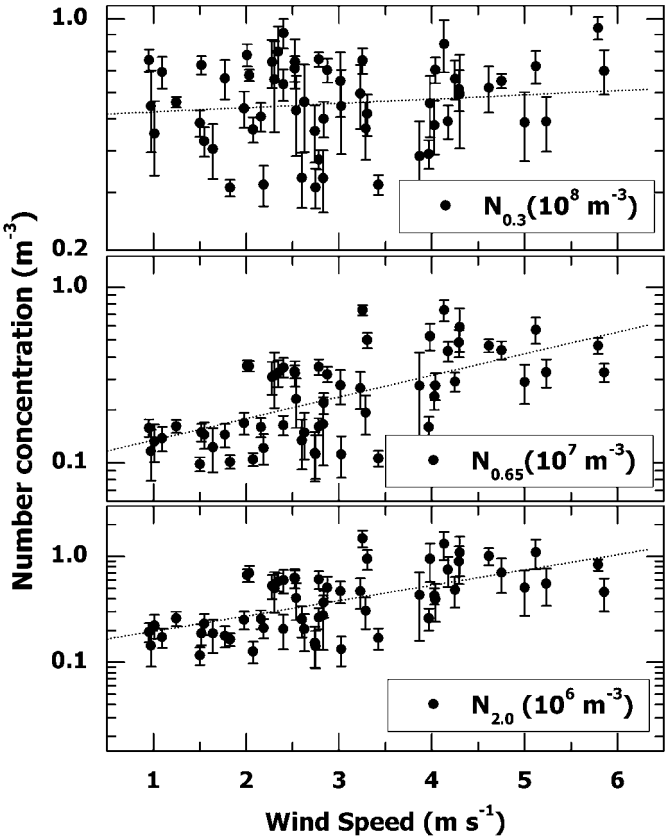


**Fig. 11.** Scatter plot of wind speed versus number concentration of particle diameter greater than 0.3 $\mu$m ($N_{0.3}$), 0.65 $\mu$m ($N_{0.65}$) and 2.0 $\mu$m ($N_{2.0}$) are shown in the panels top to bottom, respectively.



ACPD
8, 15855–15899, 2008



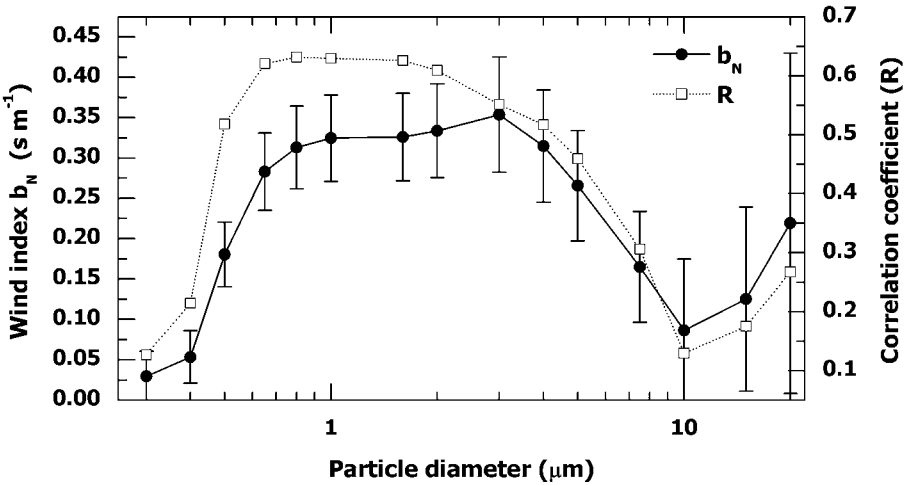


**Fig. 12.** Size segregated wind index (*b*) of number concentration on the left abscissa and corresponding correlation coefficient on right abscissa.



ACPD
8, 15855–15899, 2008



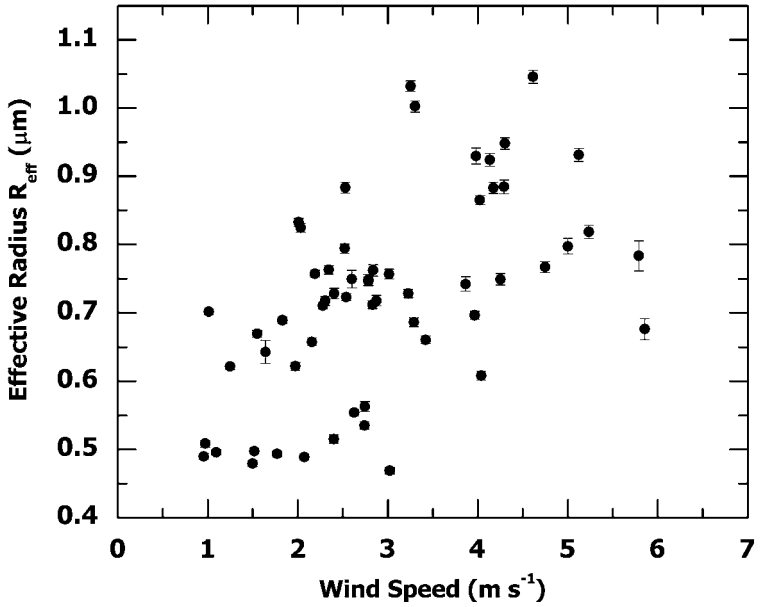


**Fig. 13.** Scatter diagram of wind speed ($U_{10}$) versus effective radius ($R_{eff}$).



ACPD
8, 15855–15899, 2008



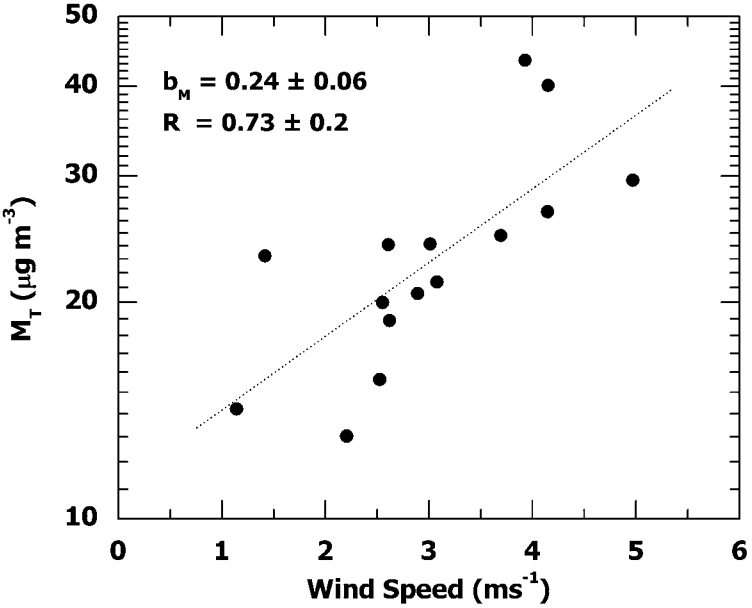


**Fig. 14.** Scatter diagram of total mass concentration versus wind speed.



ACPD
8, 15855–15899, 2008



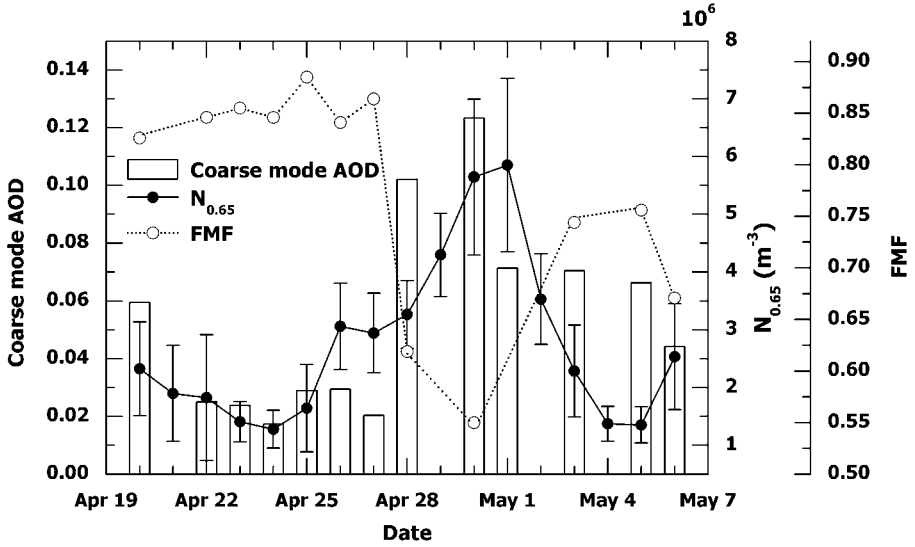


**Fig. 15.** Temporal variation of coarse mode AOD and number concentration of particle diameter greater than 0.65 $\mu$m are shown in the upper panel along the left and right ordinates, respectively.



ACPD
8, 15855–15899, 2008



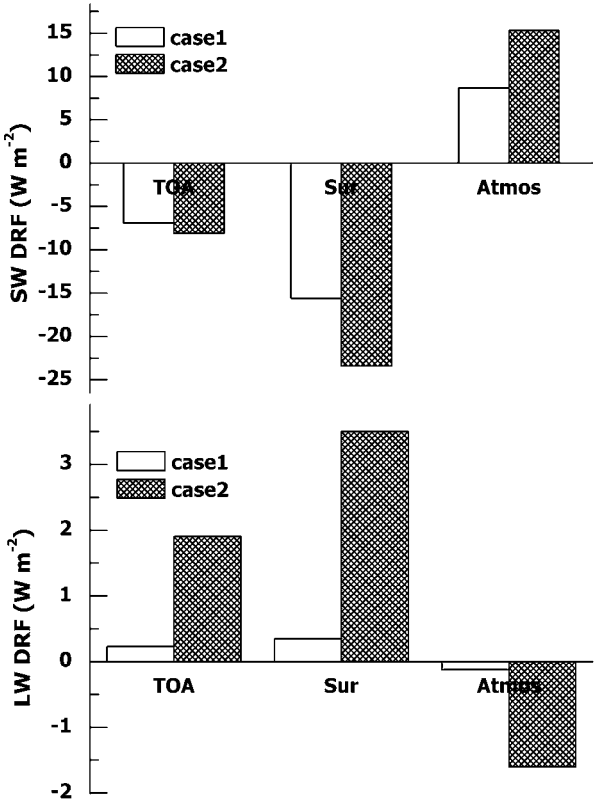


**Fig. 16.** Aerosol radiative forcing estimated for longwave and short wave regime of solar spectrum for the surface, top of the atmosphere and with the atmosphere.



ACPD
8, 15855–15899, 2008